

A novel GPU-based sonar simulator for real-time applications

Abstract

Sonar simulation requires great computational effort due to the complexity of acoustic physics mainly when applied in the underwater environment. This fact turns the reproduction of sensor data into a non-trivial task. On the other hand, simulation of sonar operation data allows to evaluate algorithms and control systems without going to the real underwater environment; that reduces the costs and risks of in-field experiments. This paper proposes a novel real-time underwater imaging sonar simulator, which uses the OpenGL shading language (GLSL) chain on graphics processing unit (GPU), and is able to simulate two main types of sonar sensors: mechanical scanning imaging sonars (MSIS) and forward-looking sonars (FLS). The virtual underwater simulation was conceived based on three frameworks: (i) OpenSceneGraph (OSG) reproduces the ocean visual effects, (ii) Gazebo deals with physics effects, and (iii) the Robot Construction Kit (Rock) controls the sonar in underwater environments. The proposed sonar simulation exploits the rasterization pipeline in order to build a matrix comprised of echo intensity, distance and angular distortion, being all calculated over objects shapes in the 3D rendered scene. Sonar-intrinsic speckle noise and surface reflectance property are also considered as part of the acoustic image. Our evaluation demonstrated that the proposed method is able to operate with high frame rate, as well as realistic sonar image quality in different virtual underwater scenarios.

Key words: Simulated sensor data, sonar imaging, GPU-based processing, Robot Construction Kit (Rock), Underwater robotics.

1. Introduction

1 Simulation is an useful tool for designing and programming
2 autonomous robot systems. That allows evaluating robot behav-
3 ior, without dealing with physical hardware or decision-making
4 algorithms and control systems in real-time trials, as well as
5 costly and time-consuming field experiments.

6 When working with autonomous underwater vehicles (AUVs),
7 simulation of facilities are specially relevant. AUVs usually de-
8 mand expensive hardware and perform long-term data gather-
9 ing operations, taking place in restrictive sites. As AUV does
10 not need umbilical cable, and the underwater communication
11 carries on by unreliable acoustic links, the robot should be able
12 to make completely autonomous decisions, even with low-to-
13 zero external assistance. While the analysis and interpretation
14 of sensor data can be performed in a post-processing step, a
15 real-time simulation is strongly needed for testing and evalua-
16 tion of vehicle's motion responses, avoiding involved risks on
17 real world rides.

18 AUVs usually act below the photic zone, with high turbid-
19 ity and huge light scattering. This makes the quality of image
20 acquisition by optical devices limited by a short range, and also
21 artificially illuminated and clear visibility conditions. To tackle
22 with that limitations, high-frequency sonars have been used pri-
23 marily on AUVs' navigation and perception systems. Acoustic
24 waves emitted by sonars are significantly less affected by water
25 attenuation, aiding operation at greater ranges even as low-to-
26 zero visibility conditions, with a fast refresh rate. Although
27 sonar devices usually solve the main shortcomings of optical
28 sensors, they provide noisy data of lower resolution and more
29 difficult interpretation.

30 By considering sonar benefits and singularities along with

32 the need to evaluate AUVs, recent works proposed ray tracing-
33 and tube tracing-based techniques to simulate acoustic data with
34 very accurate results, although having a high computational
35 cost [1, 2, 3, 4, 5, 6, 7]. Bell [1] proposed a simulator based
36 on optical ray tracing for underwater side-scan sonar imagery;
37 images were generated by acoustic signals represented by rays,
38 which are repeatedly processed, forming a 2D-array. Coiras and
39 Groen [2] used frequency-domain signal processing to produce
40 synthetic aperture sonar frames; in that method, the acoustic
41 image was created by computing the Fourier transform of the
42 acoustic pulse used to insonify the scene. For forward-looking
43 sonar simulations, Guériot and Sintes [3] introduce a volume-
44 based approach of energy interacting with the scene, and col-
45 lected by the receiving sonar; the sound propagation is defined
46 by series of acoustic tubes, being always orthogonal to the cur-
47 rent sonar view, where the reverberation and objects surface ir-
48 regularities are also addressed. Saç *et al.* [4] described a sonar
49 model by computing the ray tracing in frequency domain; when
50 a ray hits an object in 3D space, three parameters are calcu-
51 lated to process the acoustic data: the Euclidean distance from
52 the sonar axis, the intensity of returned signal by Lambert Illu-
53 mination model and the surface normal; the reverberation and
54 shadow phenomena are also considered in the scene rendering.
55 DeMarco *et al.* [5] used Gazebo and Robot Operating System
56 (ROS) [8] integration to simulate the acoustic sound pulses by
57 a ray tracing technique, and to produce a 3D point cloud of
58 the coverage area; the reflected intensity has taken account of
59 object reflectivity and the sonar image is corrupted by adding
60 Gaussian noise, salt-and-pepper noise and median blur empir-
61 ically defined. Gu *et al.* [6] modeled a forward-looking device
62 where the ultrasound beams were formed by a set of rays; the
63 acoustic image is significantly limited by its representation us-

64 ing only two colors: white, when the ray strikes an object, and
 65 black for shadow areas. Kwak *et al.* [7] evolved the previous
 66 approach by adding a sound pressure attenuation to produce the
 67 gray-scale sonar frame, while the other physical characteristics
 68 related to sound transmission are disregarded.

69 1.1. Contributions

70 This paper introduces a novel imaging sonar simulator that
 71 presents some contributions in relation to the existing approaches.
 72 Instead of simulating the sound pulse paths and the effects of
 73 their encounters with the virtual objects, as presented by the ray
 74 tracing and tube tracing-based methods [1, 2, 3, 4, 5, 6, 7], we
 75 take advantage of precomputed geometric data during the ras-
 76 terization pipeline to compute the acoustic frame. In addition,
 77 these informations are handled on GPU, accelerating the sim-
 78 ulation process and guaranteeing the usage by real-time appli-
 79 cations, in contrast to the methods found in [1, 2, 4, 5]. As op-
 80 posed to [1, 2, 3, 4, 5, 6, 7], where the proposed models simulate
 81 a specific sonar type, our model is able to reproduce two kind
 82 of sonar devices: mechanical scanning imaging sonar (MSIS)
 83 and forward-looking sonar (FLS). The intensity measured back
 84 from the insonified objects depends on surface normal direc-
 85 tions and reflectivity, producing more realistic simulated frames
 86 than binary representation as found in [6, 7]. The speckle noise
 87 is modeled as a non-uniform Gaussian distribution and applied
 88 to the final sonar image, performing a more realistic sensing,
 89 differently to [3, 4, 5, 6, 7]. On the other hand, our proposed
 90 approach introduces limitations not present in some of existing
 91 techniques, such as reverberation phenomenon [4] and additive
 92 noise model [4, 5].

93 The main goal here is to build quality and low time-consum-
 94 ing acoustic frames, according to underwater sonar image for-
 95 mation and operation modes (see Section 2). The shader matrix
 96 with depth and normal buffers, and angular distortion values are
 97 extracted from underwater scene during the rasterization pipe-
 98 line, and subsequently fused to generate the simulated sonar
 99 data, as described in Section 3. Qualitative and time evalua-
 100 tion results for two different sonar devices are presented in Section
 101 4, and allow for the use of the proposed simulator in real-time
 102 applications.

103 2. Imaging Sonar operation

104 Sonars are echo-ranging devices that use acoustic energy to
 105 locate and survey objects in a desired area. The sonar trans-
 106 ducer emits pulses of sound waves (or ping) until they hit with
 107 any object or be completely absorbed. When the acoustic sig-
 108 nal collides with a surface, part of this energy is reflected, while
 109 other is refracted. The sonar data is built by plotting the echo
 110 measured back versus time of acoustic signal. The transducer
 111 reading in a given direction forms a *beam*. A single beam trans-
 112 mitted from a sonar is illustrated in Fig. 1. The horizontal and
 113 vertical beamwidths are represented by the azimuth ψ and el-
 114 evation θ angles, respectively, where each sampling along the
 115 beam is named as *bin*. The sonar coverage area is defined by
 116 R_{min} and R_{max} . Since the speed of sound underwater is known,

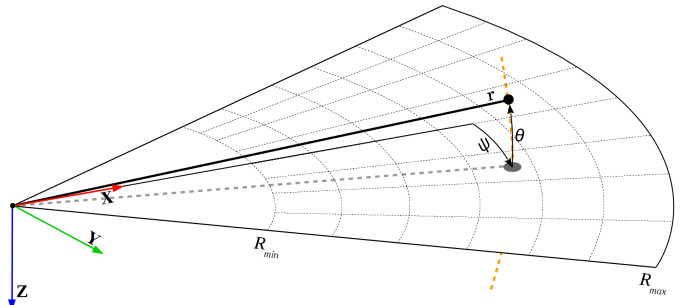


Figure 1: Imaging sonar geometry. By the projection process, all 3D points belonging to the same elevation arc (represented as dashed orange line) will be represented to the same image point in the 2D plane. In this way, range r and azimuth angle ψ are measured, and elevation angle θ is lost. The sonar coverage area is defined by R_{min} and R_{max} .

117 or can be measured, the time delay between the emitted pulses
 118 and their echoes reveal how far the objects are (distance r), as
 119 well as how fast they are moving. The backscattered acoustic
 120 power in each bin determines the intensity value.

121 With different azimuth directions, the array of transducer
 122 readings forms the final sonar image. Since all incoming sig-
 123 nals converge to the same point, the reflected echoes could have
 124 been originated anywhere along the corresponding elevation arc
 125 at a fixed range, as depicted in Fig. 1. In the acoustic represen-
 126 tation, the 3D information is lost in the projection into a 2D
 127 image.

128 2.1. Sonar characteristics

129 Although sonar devices overcome the main limitations of
 130 optical sensors, they present more difficult data interpretation
 131 due to:

- 132 (a) **Shadowing:** This effect is caused by objects blocking the
 133 sound waves transmission and causing regions behind them,
 134 without acoustic feedback. These regions are defined by a
 135 black spot in the image occluding part of the scene;
- 136 (b) **Non-uniform resolution:** The amount of pixels used to
 137 represent an intensity record in the cartesian coordinate
 138 system grows as its range increases. This fact causes im-
 139 age distortions and object flatness;
- 140 (c) **Changes in viewpoint:** Imaging the same scene from dif-
 141 ferent viewpoints can cause occlusions, shadows move-
 142 ments and significant alterations of observable objects [9].
 143 For instance, when an outstanding object is insonified, its
 144 shadow is shorter, as the sonar becomes closer;
- 145 (d) **Low signal-to-noise ratio (SNR):** The sonar suffers from
 146 low SNR mainly due the very-long-range scanning, and
 147 the presence of speckle noise introduced caused by acous-
 148 tic wave interferences [10];
- 149 (e) **Reverberation:** This phenomenon is caused when multi-
 150 ple acoustic waves returning from the same object are de-
 151 tected over the same ping, producing duplicated objects.

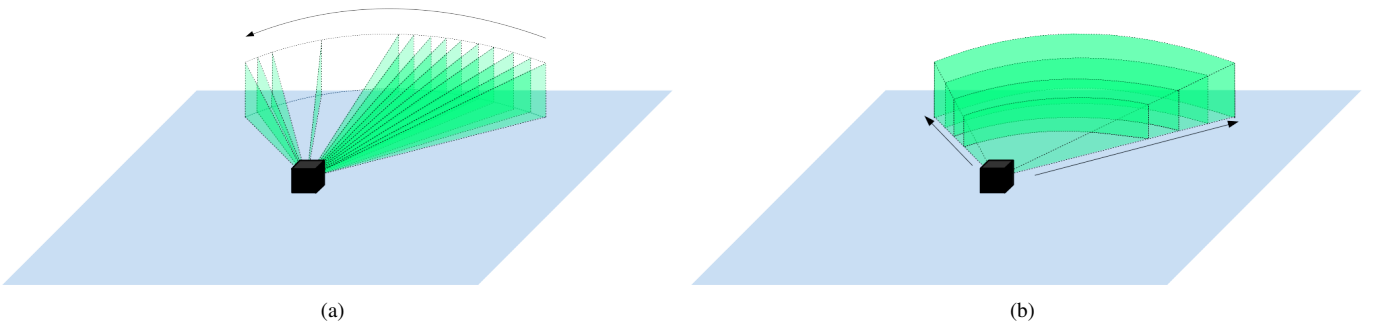


Figure 2: Different underwater sonar readings: (a) From a mechanical scanning imaging sonar and (b) from a forward-looking sonar.

152 2.2. Types of underwater sonar devices

153 The most common types of underwater acoustic sonars are
 154 MSIS and FLS. In the former, the sonar image is built for each
 155 pulse, with one beam per reading (see Fig. 2(a)); these sonar
 156 images are usually shown on a display pulse by pulse, and the
 157 head position reader is rotated according to motor step angle.
 158 After a full 360° sector reading (or the desired sector defined
 159 by left and right limit angles), the accumulated sonar data is
 160 overwritten. The acquisition of a scanning image involves a rel-
 161 atively long time, introducing distortions caused by the vehicle
 162 movements. This sonar device is generally applied in obstacle
 163 avoidance [11] and navigation [12] applications.

164 As illustrated in Fig. 2(b), the whole forward view of a FLS
 165 is scanned and the current data is overwritten by the next one
 166 in a high frame rate, with n beams being read simultaneously.
 167 This is similar to a streaming video imagery for real-time appli-
 168 cations. This imaging sonar is commonly used for navigation
 169 [13], mosaicing [9], target tracking [14] and 3D reconstruction
 170 [15].

171 3. GPU-based sonar simulation

172 The goal of this work is to simulate two types of underwa-
 173 ter sonar by vertex and fragment processing, with a low com-
 174 putational cost. The complete pipeline of the proposed simu-
 175 lator, from the virtual scene to the simulated acoustic data, is
 176 seen in Fig. 3 and is detailed in the following subsections. The
 177 sonar simulation is written in C++ with OpenCV [16] support
 178 as Rock packages.

179 3.1. Rendering underwater scene

180 The Rock-Gazebo integration [17] provides the underwa-
 181 ter scenario, and allows real-time hardware-in-the-loop simula-
 182 tions. In this framework, Gazebo handles the physical engines,
 183 and the Rock’s visualization tools are responsible by the scene
 184 rendering. The graphical data in Rock are based on OpenScene-
 185 Graph framework, an open source C/C++ 3D graphics toolkit
 186 built on OpenGL. The osgOcean framework is used to simulate
 187 the ocean visual effects, and the ocean buoyancy is defined by
 188 the Gazebo, as described in [17].

189 All scene aspects, such as world model, robot parts (in-
 190 cluding sensors and joints) and other objects presented in the
 191 environment are defined by simulation description files (SDF),

192 which use the SDFormat [18], a XML format used to describe
 193 simulated models and environments for Gazebo. Visual and
 194 collision geometries of vehicle and sensor robot are also de-
 195 scribed in specific file formats. Each component described in
 196 the SDF file becomes a Rock component, which is based on
 197 the Orococos real-time toolkit (RTT) [19], providing I/O ports,
 198 properties and operations as communication layers. When the
 199 models are loaded, Rock-Gazebo creates I/O ports to allow real-
 200 world or simulated system components interacting with the sim-
 201 ulated models. A resulting scene sample of this integration is
 202 seen in Fig. 4.

203 3.2. Shader rendering

204 GPUs are parallel numeric computing chips specialized to
 205 speed up 2D and 3D graphics processing, reducing the compu-
 206 tational effort of the central processing unit (CPU). The ren-
 207 dering pipeline can be customized by defining programs on
 208 GPU called shaders. A shader is written in OpenGL Shad-
 209 ing Language (GLSL) [20], a high-level language with a C-
 210 based syntax which enables more direct control of graphics
 211 pipeline, which avoids the use of low-level or hardware-specific
 212 languages. Shaders can describe the characteristics of either a
 213 vertex or a fragment (a single pixel). Vertex shaders are respon-
 214 sible by transforming the vertex position into a screen position
 215 by the rasterizer, generating texture coordinates for texturing,
 216 and lighting the vertex to determine each color. The rasteri-
 217 zation results in a set of pixels to be processed by fragment
 218 shaders, which manipulate their locations, depth and alpha val-
 219 ues, and interpolated parameters from the previous stages, such
 220 as colors and textures.

221 In our work, the underwater scene is sampled by a virtual
 222 camera, whose optical axis is aligned with the intended viewing
 223 direction of the imaging sonar device, as well as the covered
 224 range and opening angle. By programming the fragment and
 225 vertex shaders, the sonar data is computed as:

- 226 (a) **Depth** is the camera focal length, calculated by the Eu-
 227 clidean distance to the object surface point;
- 228 (a) **Intensity** presents the echo reflection energy based on
 229 object surface normal angle up to the camera;
- 230 (a) **Angular distortion** is the angle formed from the camera
 231 center column up to the camera boundary column, for
 232 both directions.

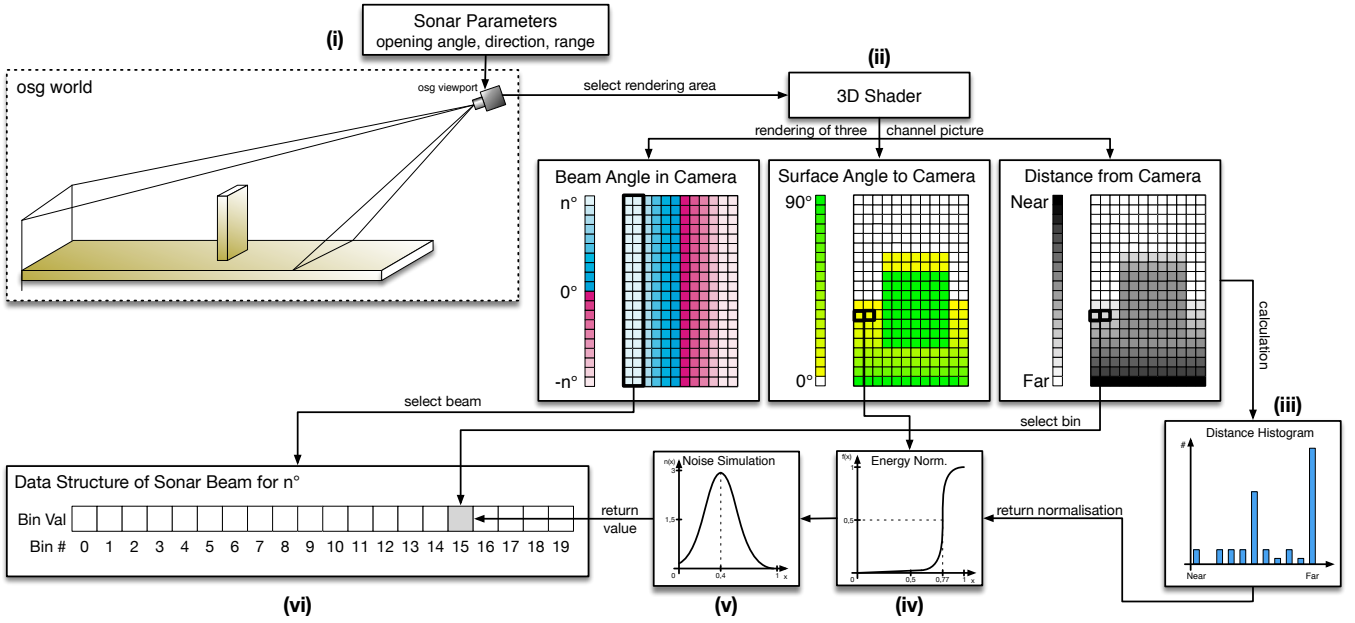


Figure 3: A graphical overview of the imaging sonar simulation process: (i) a virtual camera, specialized as the sonar device, samples the underwater scene; (ii) three components are calculated by shader rendering on GPU: the Euclidean distance from camera center, the surface normal angles, and the angular distortion; the shader information is split in beam parts, according the angular distortion values, and bin depth and intensity are defined by distance histogram (iii) and energy normalization (iv); (v) the speckle noise is applied to the final sonar data; (vi) and the simulated acoustic data is presented as Rock's data type.

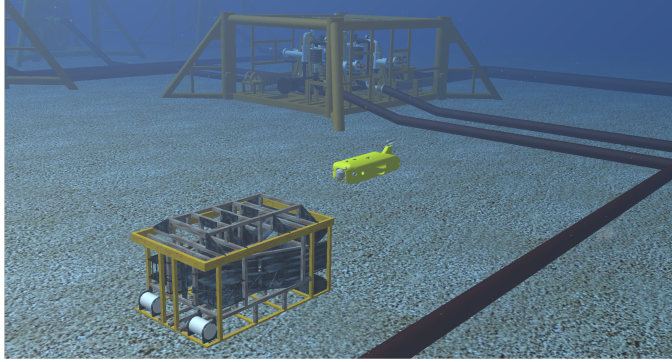


Figure 4: The AUV in Rock-Gazebo underwater scene.

250 geometry remains unchanged. Since normal maps are built in
 251 tangent space, interpolating the normal vertex and the texture, a
 252 tangent, bitangent and normal (TBN) matrices are computed to
 253 convert the normal values into the world space. Representation
 254 of normal mapping process in our approach is seen in Fig. 5.

255 The reflectance allows to properly describe the intensity re-
 256 ceived back from observable objects in shader processing, ac-
 257 cording their material properties. For instance, aluminum has
 258 more reflectance than wood and plastic. When an object has
 259 its reflectivity defined, the reflectance value ρ is passed to frag-
 260 ment shader and must be positive. As seen in Fig. 6, normal
 261 values are directly proportional to the reflectance value ρ . At
 262 the end, the shader process provides a matrix with three main
 263 data: Intensity, depth and angular distortion.

264 3.3. Simulating sonar device

265 The 3D shader matrix is processed in order to build the cor-
 266 responding acoustic representation. Since the angular distortion
 267 is radially spaced over the horizontal field-of-view, where all
 268 pixels in the same column have the same angle value, the first
 269 step is to split the image in a number of beam parts. Each col-
 270 umn is correlated with its respective beam, according to sonar
 271 bearings, as seen in Fig. 3. In this case, one beam represents
 272 one or more columns. Each beamed sub-image is converted
 273 into bin intensities using the depth and intensity data. In a real
 274 imaging sonar, the echo measured back is sampled over time
 275 and the bin number is proportional to the sensor range. In other
 276 words, the initial bins represent the closest distances, while the
 277 latest bins are the farthest ones. Therefore a distance histogram
 278 is evaluated to group the sub-image pixels with their respective

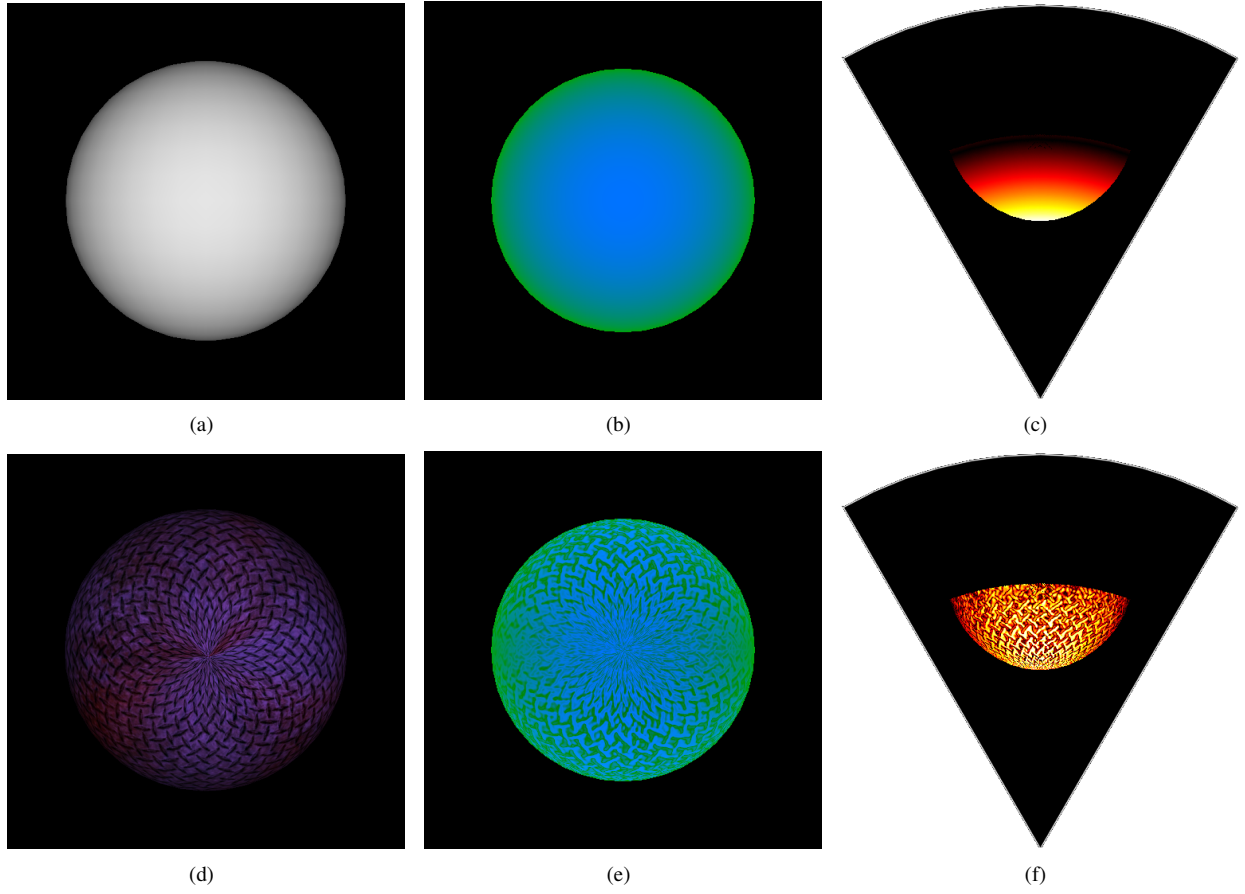


Figure 5: Example of shader rendering with normal mapping processing: A sphere without texture (a) and with texture (d); their respective shader image representation in (b) and (e), where blue is the normal channel and green is the depth one; and the final acoustic image in (c) and (f). By using normal mapping technique, the textures changes the normal directions, and the sonar image details the appearance of object surface, like in real-world sensing.

279 bins, according to the depth value. This information is used to
280 calculate the accumulated intensity of each bin.

281 Due to the acoustic beam spreading and absorption in the
282 water, the final bins have less echo strength than the first ones,
283 because the energy is lost twice, in the environment. To tackle
284 with that issue, the sonar devices use an energy normalization
285 based on time-varying gain for range dependence compensa-
286 tion, which spreads losses in the bins. In our simulation ap-
287 proach, the accumulated intensity in each bin is normalized as

$$288 \quad I_{bin} = \sum_{x=1}^N \frac{1}{N} \times S(i_x), \quad (1)$$

289 where I_{bin} is the intensity in the bin after energy normalization,
290 x is the pixel location in the shader matrix, N is the distance his-
291 togram value (number of pixels) of that bin, $S(i_x)$ is a sigmoid
292 function, and i_x is the intensity value of the pixel x .

293 Finally, the sonar image resolution needs to be big enough
294 to fill all informations of the bins. For that, the number of bins
295 involved is in direct proportion to the sonar image resolution.

296 3.4. Noise model

297 Imaging sonar systems are disturbed by a multiplicative noise
298 known as speckle, and caused by coherent processing of backscat-
299 tered signals from multiple distributed targets. These latter ones

300 degrade image quality and the visual evaluation. Speckle noise
301 results in constructive and destructive interferences which are
302 shown as bright and dark dots in the image. The noisy image
303 has been expressed as [21]:

$$304 \quad y(t) = x(t) \times n(t), \quad (2)$$

305 where t is the time instant, $y(t)$ is the noised image, $x(t)$ is the
306 free-noise image, $n(t)$ is the speckle noise matrix, and \times symbol
307 defines an element-wise multiplication.

308 This type of noise is well-modeled as a Gaussian distri-
309 bution. The physical explanation is provided by the central
310 limit theorem, which states that the sum of many independent
311 and identically distributed random variables tends to behave a
312 Gaussian random variable. A Gaussian distribution is defined
313 by following a non-uniform distribution, skewed towards low
314 values, as seen in Fig. 3, and applied as speckle noise in the
315 simulated sonar image. After that, the simulation sonar data
316 process is performed in each frame.

317 3.5. Integrating sonar device with Rock

318 To export and display the sonar image, the simulated data
319 is encapsulated as Rock's sonar data type, and provided as an
320 output I/O port of a Rock's component.

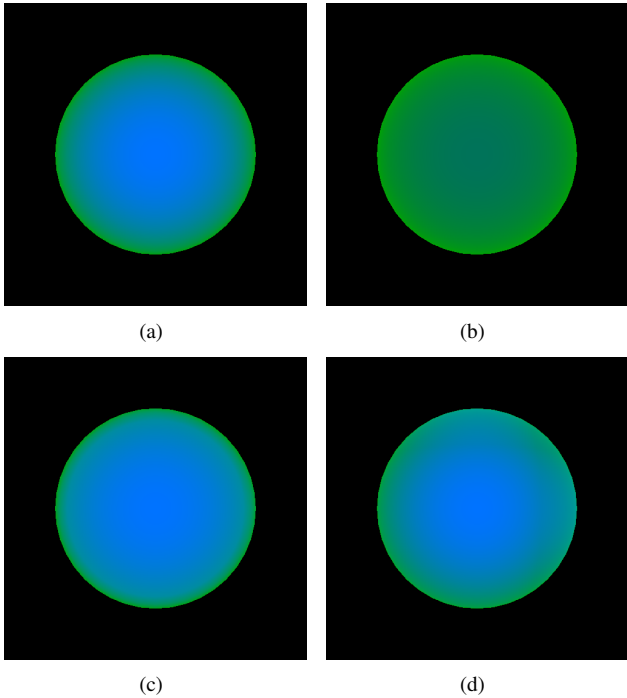


Figure 6: Examples of different reflectance values, ρ , applied in shader image representation, where blue is the normal channel and green is the depth channel: (a) raw image; (b) $\rho = 0.35$; (c) $\rho = 1.40$; and (d) $\rho = 2.12$.

4. Simulation results and experimental analysis

To evaluate our simulator, experiments were conducted by using a 3D model of an AUV equipped with one MSIS and one FLS, studied in different scenarios. The following device configurations are summarized in Table 1. As the scene frames are being captured by the sonars, resulting simulated acoustic images are sequentially presented, on-the-fly.

4.1. Experimental evaluation

The virtual FLS from AUV was used to insonify the scenes from three distinct scenarios. A docking station, in parallel with a pipeline on the seabed, composes **the first scenario** (see Fig. 7(a)). The target surface is well-defined in the simulated acoustic frame (see Fig. 7(b)), even as the shadows and speckle noise. Given the docking station is metal-made, the texture and reflectivity were set, such as a higher intensity shape was resulted in comparison with the other targets. **The second scenario** presents the vehicle in front of a manifold model in a non-uniform seabed (see Fig. 7(c)). The target model was insonified to generate the sonar frame from the underwater scene. The frontal face of the target, as well the portion of the seabed and the degraded data by noise, are clearly visible in the FLS image. Also, a long acoustic shadow is formed behind the manifold, occluding part of the scene. **The third scenario** contains a sub-sea isolation valve (SSIV) structure, connected to a pipeline in the bottom (see Fig. 7(e)).

Due to sensor configuration and robot position, the initial bins usually present a blind region in the three simulated scenes,

Table 1: Sonar device configurations used on experimental evaluation.

Device	# of beams	# of bins	Field of view	Down tilt	Motor Step
FLS	256	1000	120° x 20°	20°	-
MSIS	1	500	3° x 35°	0°	1.8°

caused by absence of objects at lower ranges, similar to real images. Also, the brightness of sea-floor decreases, when farthest from sonar, because of the normal orientation of the surface.

The MSIS was also simulated in three different experiments. The robot in a big textured tank composes **the first scene** (see Fig. 8(a)). Similar to the first scenario of FLS experiment, the reflectivity and texture were set to the target. The rotation of the sonar head position, by a complete 360° scanning, produced the acoustic frame of tank walls (see Fig. 8(b)). **The second scene** involves the vehicle's movement during the data acquisition process. The scene contains a grid around the AUV (see Fig. 8(c)), a MSIS in the front of the AUV is used. This trial induces a distortion in the final acoustic frame, because the relative sensor position with respect to the surrounding object changes while the sonar image is being built (see Fig. 8(d)). In this case, the robot rotates 20° left during the scanning. **The last scene** presents the AUV over oil and gas structures on the sea bottom (see Fig. 8(e)). Using a MSIS located in the back of the AUV, with a vertical orientation, the scene was scanned to produce the acoustic visualization. As illustrated in Fig. 8(f), object surfaces present clear definition in the slice scanning of the sea-floor.

The experimental scenarios provided enough variability of specific phenomena usually found in real sonar images, such as acoustic shadows, noise interference, surface irregularities and properties, distortion during the acquisition process and gradient of acoustic intensities. However, our sonar model also presented some limitations. For instance, the speckle noise application is restricted to regions with acoustic intensity, as shown in Figs. 7(f) and 8(b). This fact is due to our sonar model, defined in Eq. 2, be multiplicative. In real sonar images, the noise also granulates the shadows and blind regions. The sonar simulator can be improved by inserting an additive noise to our model. A second feature missing in simulated acoustic images are the ghost effects caused by reverberation. This lacking part can be addressed by implementation of a multi-path propagation model.

4.2. Computational time

Performance evaluation of the simulator was determined by considering the suitability to run real-time applications. The experiments were performed on a laptop with Ubuntu 16.04 64 bits, Intel Core i7 3540M processor running at 3 GHz with 16GB DDR3 RAM memory and NVIDIA NVS 5200M video card.

The elapsed time of each sonar data is stored to compute the average time, standard deviation and frame rate metrics, after

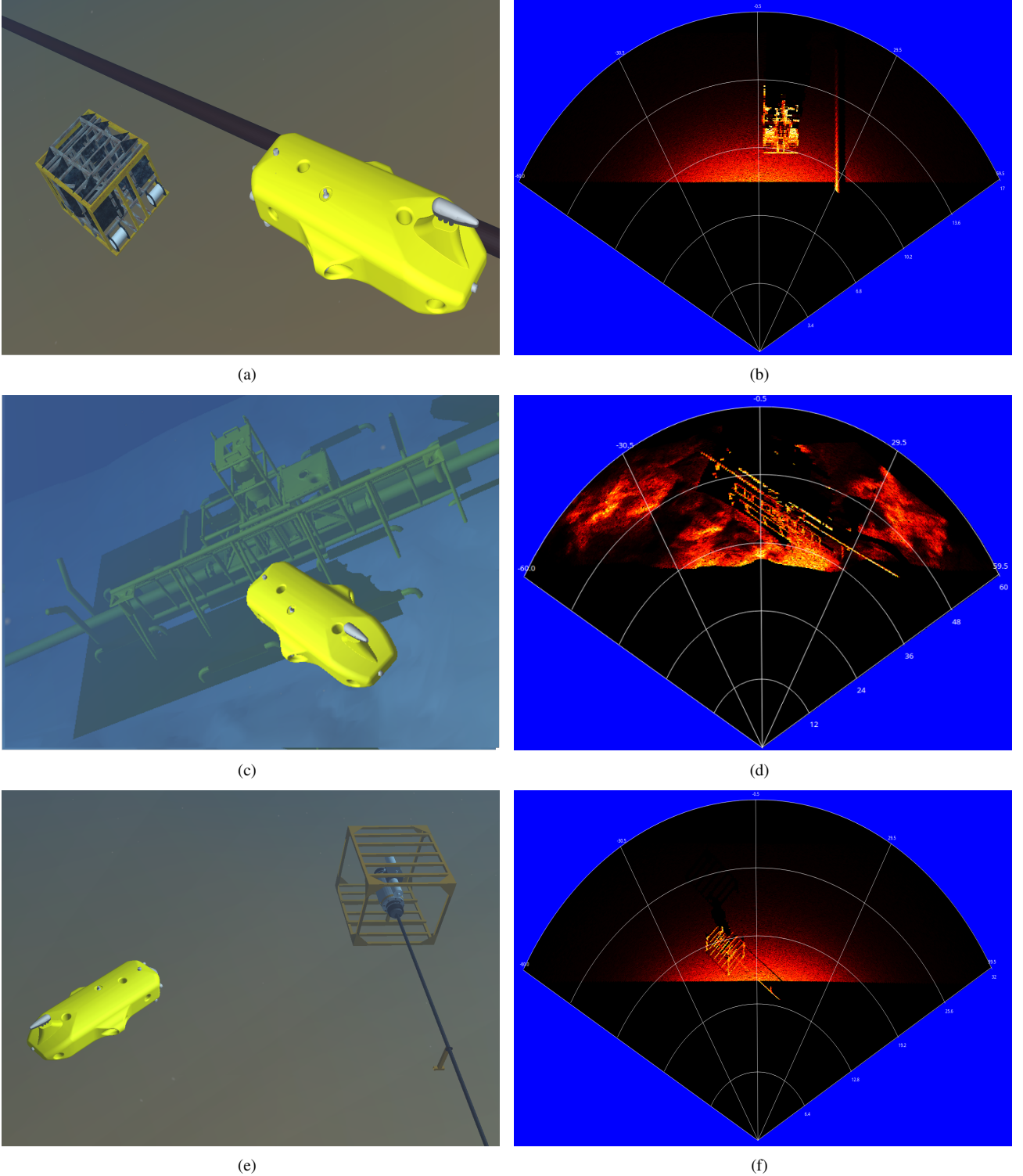


Figure 7: Forward-looking sonar simulation experiments: (a), (c) and (e) present the virtual underwater trials, while (b), (d) and (f) are the following acoustic representations of each scenario, respectively.

500 iterations, as summarized in Tables 2 and 3. After changing the device parameters, such as number of bins, number of beams and field of view, the proposed approach generated the sonar frames with a high frame rate, for both sonar types. Given the Tritech Gemini 720i, a real forward-looking sonar sensor,

with a field of view of 120° by 20° and 256 beams, presents a maximum update rate of 15 frames per second, the results allow the use of the sonar simulator for real-time applications. Also, the MSIS data built by the simulator is able to complete a 360° scan sufficiently fast in comparison with a real sonar as Tritech

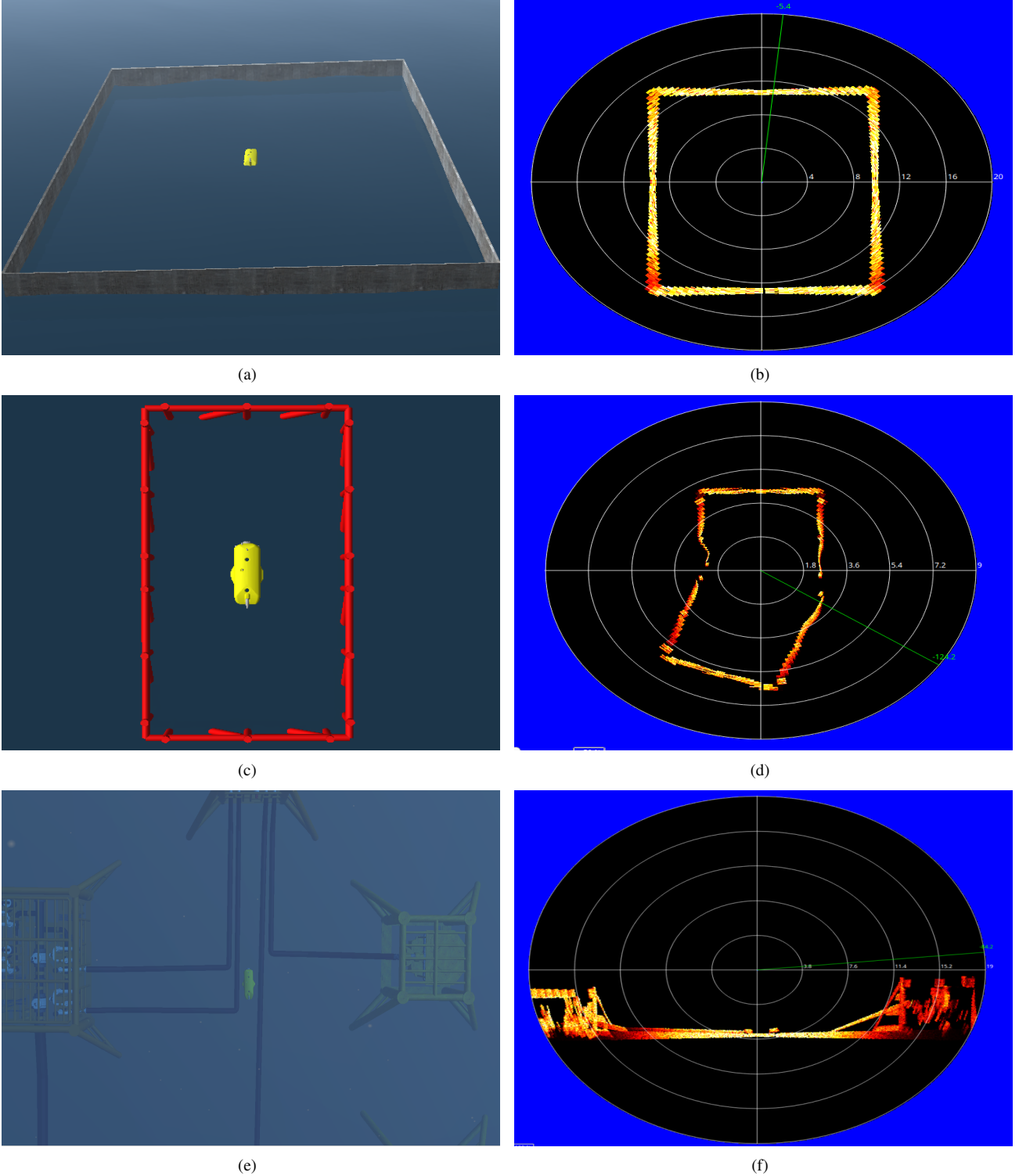


Figure 8: Experiments using mechanical scanning imaging sonar in three different scenarios (a), (c) and (e), and the respective processed simulated frames in horizontal axis in (b) and (d), and vertical axis in (f).

404 Micron DST. Moreover, for the FLS device, these rates are su-
 405 perior to the rates lists by DeMarco *et al* [5] (330ms) and Saç
 406 *et al* [4] (2.5min). For MSIS type, to the best of our knowledge,
 407 there is no previous work done for comparison.

408 According to previous results, since the number of bins is

409 directly proportional to sonar image resolution, as explained in
 410 Section 3.3, this is also correlated with the computational time.
 411 When the number of bins increases, the simulator will have a
 412 bigger scene frame to compute, and generate the sonar data.

Table 2: Processing time to generate forward-looking sonar frames with different parameters.

# of samples	# of beams	# of bins	Field of view	Average time (ms)	Std dev (ms)	Frame rate (fps)
500	128	500	120° x 20°	54.7	3.7	18.3
500	128	1000	120° x 20°	72.3	8.9	13.8
500	256	500	120° x 20°	198.7	17.1	5.0
500	256	1000	120° x 20°	218.2	11.9	4.6
500	128	500	90° x 15°	77.4	11.8	12.9
500	128	1000	90° x 15°	94.6	10.2	10.6
500	256	500	90° x 15°	260.8	18.5	3.8
500	256	1000	90° x 15°	268.7	16.7	3.7

Table 3: Processing time to generate mechanical scanning imaging sonar samples with different parameters.

# of samples	# of bins	Field of view	Average time (ms)	Std dev (ms)	Frame rate (fps)
500	500	3° x 35°	8.8	0.7	113.4
500	1000	3° x 35°	34.5	1.6	29.0
500	500	2° x 20°	10.3	0.6	96.7
500	1000	2° x 20°	41.7	3.7	24.0

5. Conclusion and future work

A GPU-based approach for imaging sonar simulation is presented here. The same model was able to reproduce the operation mode of two different types of sonar devices (FLS and MSIS) over different scenarios. The real sonar image singularities, such as multiplicative noise, surface properties and acoustic shadows are addressed and represented in the simulated frames. Specially for the shadows, the acoustic representation can present information as useful as the insonified object. Considering the qualitative results, the sonar simulator can be used by feature detection algorithms, based on corners, lines and shapes. Also, the computation time to build one sonar frame was calculated using different device settings. The vertex and fragment processing during the underwater scene rendering accelerates the sonar image building, and the metrics, such as the average time, demonstrated that the performance is much close to real imaging devices. These results allowed the use of this imaging sonar simulator by real-time applications, such as obstacle detection and avoidance, and object tracking. Finally, the reverberation effect is still missing on our simulator to perform a more realistic sensing. The future inclusion of this phenomenon will probably change the reflected intensity model and the computation time must be considered again. Next steps will focus on expand the underwater acoustic characteristics, such as additive noise and reverberation, and qualitative and computation efficiency evaluations with other imaging sonar simulators and real images.

References

- [1] Bell JM. Application of optical ray tracing techniques to the simulation of sonar images. *Optical Engineering* 1997;36(6):1806–13.
- [2] Coiras E, Groen J. Simulation and 3d reconstruction of side-looking sonar images. In: Silva S, editor. *Advances in Sonar Technology*; chap. 1. In-Tech; 2009, p. 1–15.
- [3] Guériot D, Sintes C. Forward looking sonar data simulation through tube tracing. In: MTS/IEEE OCEANS Conference. 2010, p. 1–6.
- [4] Saç H, Leblebicioğlu K, Bozdağı Akar G. 2d high-frequency forward-looking sonar simulator based on continuous surfaces approach. *Turkish Journal of Electrical Engineering and Computer Sciences* 2015;23(1):2289–303.
- [5] DeMarco K, West M, Howard A. A computationally-efficient 2d imaging sonar model for underwater robotics simulations in Gazebo. In: MTS/IEEE OCEANS Conference. 2015, p. 1–8.
- [6] Gu J, Joe H, Yu SC. Development of image sonar simulator for underwater object recognition. In: MTS/IEEE OCEANS Conference. 2013, p. 1–6.
- [7] Kwak S, Ji Y, Yamashita A, Asama H. Development of acoustic camera-imaging simulator based on novel model. In: IEEE International Conference on Environment and Electrical Engineering (EEEIC). 2015, p. 1719–24.
- [8] Quigley M, Conley K, Gerkey BP, Faust J, Foote T, Leibs J, et al. ROS: an open-source robot operating system. In: Workshop on Open Source Software, held at IEEE International Conference on Robotics and Automation (ICRA). 2009, p. 1–6.
- [9] Hurtós N. Forward-looking sonar mosaicing for underwater environments. Ph.D. thesis; Universitat de Girona; 2014.
- [10] Abbot J, Thurstone F. Acoustic speckle: theory and experimental analysis. *Ultrasonic Imaging* 1979;1(4):303–24.
- [11] Ganesan V, Chitre M, Brekke E. Robust underwater obstacle detection and collision avoidance. *Autonomous Robots* 2015;40(7):1–21.
- [12] Ribas D, Rida P, Neira J. Underwater SLAM for structured environments using an imaging sonar. Springer-Verlag Berlin Heidelberg; 2010.
- [13] Fallon MF, Folkesson J, McClelland H, Leonard JJ. Relocating underwater features autonomously using sonar-based SLAM. *Journal of Ocean Engineering* 2013;38(3):500–13.
- [14] Liu L, Xu W, Bian H. A LBF-associated contour tracking method for underwater targets tracking. In: MTS/IEEE OCEANS Conference. 2016, p. 1–5.
- [15] Huang TA, Kaess M. Towards acoustic structure from motion for imaging sonar. In: IEEE/RSJ International Conference on Intelligent Robots and Systems (IROS). 2015, p. 758–65.
- [16] Bradski G. The opencv library. *Doctor Dobbs Journal* 2000;25(11):120–

- 484 6.
- 485 [17] Watanabe T, Neves G, Cerqueira R, Trocoli T, Reis M, Joyeux S, et al.
486 The Rock-Gazebo integration and a real-time AUV simulation. In: IEEE
487 Latin American Robotics Symposium (LARS). 2015, p. 132–8.
- 488 [18] SDF. <http://sdformat.org/>; 2017. Accessed: 2017-04-23.
- 489 [19] Soetens P, Bruyninckx H. Realtime hybrid task-based control for robots
490 and machine tools. In: IEEE International Conference on Robotics and
491 Automation (ICRA). 2005, p. 260–5.
- 492 [20] Rost RJ, Licea-Kane B, Ginsburg D, Kessenich JM, Lichtenbelt B, Malan
493 H, et al. OpenGL shading language. 3rd ed.; Addison-Wesley Profes-
494 sional; 2009.
- 495 [21] Lee J. Digital image enhancement and noise filtering by use of local sta-
496 tistics. IEEE Transactions on Pattern Analysis and Machine Intelligence
497 1980;2(2):165–8.